J. Ocean Univ. China (Oceanic and Coastal Sea Research)
https://doi.org/10.1007/s11802-019-3854-1
ISSN 1672-5182, 2019 18 (4): 823-833
http://www.ouc.edu.cn/xbywb/
E-mail:xbywb@ouc.edu.cn

Performance Evaluation of Bottom-Standing Submerged Breakwaters in Regular Waves Using the Meshless Singular Boundary Method

SENOUCI Fawzi[1), 3)], CHIOUKH Nadji[1), 2), *], and DRIS Mohammed El-Amine[1), 3)]

1) *Department of Hydraulics*, *University Djillali Liabes of Sidi Bel-Abbes*, *Sidi Bel-Abbes* 22000, *Algeria*
2) *Laboratory of Naval Aero-Hydrodynamics*, *USTO MB*, *Oran* 31000, *Algeria*
3) *Laboratory of Civil Engineering and Environment*, *University Djillali Liabes of Sidi Bel-Abbes*, *Sidi Bel-Abbes* 22000, *Algeria*

(Received March 29, 2018; revised August 19, 2018; accepted October 23, 2018)

Abstract In this paper, the improved version of the meshless singular boundary method (ISBM) is developed for analyzing the hydrodynamic performance of bottom-standing submerged breakwaters in regular normally incident waves. Both the single and dual prismatic breakwaters of rectangular and trapezoidal forms are examined. Only the impermeable breakwaters are considered in this study. The physical problem is cast in terms of the Laplace equation governing an irrotational flow and incompressible fluid motion with the appropriate mixed-type boundary conditions, and it is solved numerically using the ISBM. The numerical results are presented in terms of the hydrodynamic quantities of reflection and transmission coefficients. The values are first validated against the data of previous studies, computed, and discussed for a variety of structural conditions, including the height, width, and spacing of breakwater submergence. An excellent agreement is observed between the ISBM results and those of other methods. The breakwater width is found to feature marginal effects compared with the height. The present method is shown to accurately predict the resonant conditions at which the maximum reflection and transmission occur. The trapezoidal breakwaters are found to generally present a wide spectrum of reflections, suggesting that they would function better than the rectangular breakwaters. The dual breakwater systems are confirmed to perform much better than single structures.

Key words meshless improved singular boundary method; regular normal waves; rectangular and trapezoidal breakwaters; reflection; transmission

1 Introduction

The submerged breakwaters are popular structures used to safeguard coastal areas in situations where complete protection from waves is unnecessary. These structures reduce the wave energy by reflecting most of the incident waves, hence reducing the wave transmission. The submerged breakwaters can effectively create calmer areas in their leeward side similar to those in harbor entrances and marinas and possess the capability to decrease the sediment transport capacity. At the same time, the fish passage and exchange of waters between the sea and shore sides of submerged breakwaters is incompletely inhibited. If well-designed, the submerged breakwaters can offer potentially cost-effective solutions.

To identify the resonant conditions at which maximum reflections, which are widely known as Bragg resonant reflections, would occur, the wave interactions with submerged breakwaters have been studied both experimentally and theoretically.

Dattatri *et al.* (1978) conducted a comprehensive laboratory investigation to evaluate the performance characteristics of the submerged breakwaters of various types and shapes. They observed that the breakwater crest width and depth of submergence are important parameters that influence the performance of the submerged breakwaters. Abul-Azm (1994) developed an analytical solution based on the eigenfunction expansion method (EFEM) and potential flow linear theory to study the interaction of monochromatic oblique waves and impermeable submerged wide breakwater. The theoretical results were presented to show the effect of different wave and structural parameters on the transmitted and reflected waves and the hydrodynamic loadings on the breakwater. The results of the solution showed good agreement with the corresponding experimental findings and approximate analytical expressions obtained by other investigators. Hsu *et al.* (2002) carried out a series of laboratory experiments to compare the wave reflections from sandbars of rectangular, cosine, and triangular shapes. They showed that the rectangular sandbars generate the highest reflec-

* Corresponding author. E-mail: chioukh.nadji@hotmail.com

tions. Cho *et al.* (2004) carried out a series of experimental tests in a laboratory and separately developed an analytical solution based on the EFEM to investigate the wave reflection from rectangular and trapezoidal impermeable submerged breakwaters. The analytical and experimental results exhibited a good agreement and the trapezoidal shape breakwater was recommended for an overall desirable performance. Twu and Liu (2004) investigated the wave damping characteristics of a periodic array of porous bars using the EFEM. The effect of the porosity was found to further reduce both the reflection and transmission and increase the wave dissipation. Liu *et al.* (2016) recently conducted experimental laboratory tests and independently developed complete analytical linear potential solutions using the multipole expansion method for Bragg reflections of obliquely and normally incident water waves by a series of submerged semi-circular bars lying on the bed. An overall reasonable agreement was observed between the analytical results and the experimental data. Similarly, Zhao *et al.* (2017) developed an analytical solution based on the EFEM for oblique wave scattering by a submerged porous breakwater with a leeside partially reflecting vertical wall.

Numerical methods have also been applied successfully in the study of submerged breakwaters. The most popular domain type methods comprise the finite element method and finite volume method. These methods involve meshing over the domain and special integration over the elements. On the other hand, boundary-type methods employ singular kernels to circumvent the physical domain and therefore only require solution on the domain boundary. These methods include the boundary element method (BEM), and meshless methods, such as the method of fundamental solutions (MFS), regularized meshless method (RMM), and singular boundary method (SBM). The MFS, RMM, and SBM are advantageous as only source nodes are distributed on the domain boundary, contrary to the BEM, which requires meshing using boundary elements. Moreover, in meshless methods (MFS, RMM, and SBM) discretization of the equations governing the physical problem involves only the singular kernels to find simple relations between the boundary nodes, whereas the BEM discretization requires intricate mathematics and difficult numerical integration of the singular kernels over the mesh elements. The MFS is a classical method that has been around for several decades. Fairweather and Karageorghis (1998) provide a comprehensive review of the method. The MFS uses single-layer potentials as its kernel (basis) functions. To avoid the singularity of the kernels when the source and collocation points coincide, the sources are placed on a nonphysical (fictitious) boundary other than the physical one. This condition is a major drawback of the method. To remedy the MFS, Young *et al.* (2005) proposed the RMM. This method uses double-layer potentials as kernel functions and the same physical boundary for both collocation and source points. To remove the hyper-singularities of the kernels upon the coincidence of the collocation and source points, a desingularization process is introduced by using the regularization technique of the subtracting and adding-back methods. However, the regularization of the singularities in the double-layer potentials can affect the method accuracy. The SBM is another recent meshless method proposed by Chen and Wang (2010) and Chen and Fu (2010). This method uses single-layer potentials as its kernel functions and the same physical boundary for both collocation and source points. The desingularization of the kernel functions is carried out by introducing the concept of the origin intensity factors. In the traditional SBM, the origin intensity factors are evaluated by an inverse interpolation technique. However, to carry out this technique, the SBM requires a cluster of sample nodes within the physical domain. The solution accuracy may be sensitive to the location of the sample nodes. To overcome the shortcoming of the sample nodes Chen and Gu (2012), Gu *et al.* (2012) and Gu and Chen (2013, 2014) proposed an improved version of the original SBM (ISBM). In this method the desingularization is carried out by the regularization technique of subtracting and adding-back and an improved inverse interpolation technique that requires no sample nodes.

Koley *et al.* (2015b) studied by a suitable combination of the EFEM and BEM oblique-wave scattering and trapping by bottom-standing porous breakwaters on a sloping bed. In another investigation, Koley *et al.* (2015a) studied oblique-wave trapping by bottom-standing and surface-piercing porous structures in front of a vertical rigid wall using the EFEM and separately, the multi-domain BEM. Chen *et al.* (2011) successfully applied the RMM to solve the problem of obliquely incident water waves past a single submerged breakwater with rigid and absorbing boundary conditions. Ouyang *et al.* (2016) developed a numerical solution based on the RMM to study the Bragg reflections for a train of surface water waves from a series of impermeable submerged bottom breakwaters. Chen *et al.* (2014) made the first attempt to test the feasibility of the ISBM to a two-dimensional (2D) problem of obliquely incident water waves past a submerged breakwater. Fu *et al.* (2015) applied the ISBM to various exterior wave problems. The efficiency of the method was confirmed by several numerical tests. Li *et al.* (2016) applied the ISBM to investigate the interaction of obliquely incident water waves past single and dual submerged breakwaters with rigid and absorbing boundary conditions. A dual breakwater system was found to trap more water wave energy than a single breakwater one.

The present paper aims to develop a numerical model based on the ISBM and non-viscous flow theory to analyze numerically the performance of bottom-standing single or dual submerged impermeable breakwaters in regular normally incident waves. The breakwaters are of rectangular and trapezoidal forms. The effects of several parameters relating to the geometry of the breakwaters (submergence height and width) are examined.

2 Formulation of the Problem

In this study, we consider single and dual bottom-

standing submerged impermeable breakwaters of rectangular and trapezoidal shapes as shown in Fig.1. For the sake of generality, the method is developed for a system of dual trapezoidal breakwaters.

Fig.2 shows the idealized geometry of a 2D problem in a Cartesian system (x-y). The regular normal waves of small amplitude a, period T, and wavelength L impinge from the left in water of depth d. Assuming an irrotational flow and incompressible fluid motion, the problem is formulated using a velocity potential $\Phi(x, y, t) = \mathrm{Re}[\phi(x, y)\exp(-\mathrm{i}\sigma t)]$, where Re denotes the real part, $\phi(x, y)$ refers to the time-independent spatial velocity potential, $\mathrm{i} = \sqrt{-1}$, $\sigma = 2\pi/T$ is the wave angular frequency, and t is the time. The wave number $k = 2\pi/L$ corresponds to the solution of the dispersion relation $gk\tanh(kd) = \sigma^2$, where g is the gravitational acceleration. The wave field is completely specified if the 2D velocity potential ϕ is known.

The breakwaters feature a height h, bottom width w_b, and top width w_t. For rectangular breakwaters, $w_b = w_t = w$. The dual breakwaters are separated by a distance X_S measured from the centers of the breakwaters. The total fluid domain is divided in three regions, as shown in Fig.2. Region I at $(-\infty)$ denotes the region with incoming (inflow) waves, and region III at $(+\infty)$ is where the waves are transmitted (outflow). Region II lies between regions I and III and is delimited by the rigid (impermeable) walls of the breakwaters (Γ_{b1}, Γ_{b2}, and Γ_{b3} for the front breakwater 1 and Γ_{b4}, Γ_{b5}, and Γ_{b6} for the back breakwater 2), the free surface boundary Γ_f, the seabed boundary Γ_s, and the radiation boundaries Γ^- and Γ^+ of the inflow and outflow regions, respectively. The spatial velocity potential ϕ satisfies the following conditions:

$$\frac{\partial^2\phi}{\partial x^2} + \frac{\partial^2\phi}{\partial y^2} = 0, \text{ in the fluid region II}, \quad (1)$$

$$\frac{\partial\phi}{\partial n} - \frac{\sigma^2}{g}\phi = 0,\ y = d \text{ (free surface boundary } \Gamma_f), \quad (2)$$

$$\frac{\partial\phi}{\partial n} = 0,\ y = 0 \text{ (seabed boundary } \Gamma_s), \quad (3)$$

$$\frac{\partial\phi}{\partial n} = 0,\ (x, y) \in \Gamma_{b1} + \Gamma_{b2} + \Gamma_{b3} + \Gamma_{b4} + \Gamma_{b5} + \Gamma_{b6},$$

$$\text{(breakwaters boundaries } \Gamma_b), \quad (4)$$

where n is the normal to the boundary pointing out of the flow region and $\Gamma_b = \Gamma_{b1} + \Gamma_{b2} + \Gamma_{b3} + \Gamma_{b4} + \Gamma_{b5} + \Gamma_{b6}$ denotes the total rigid (impermeable) boundaries of the breakwaters.

The radiation conditions at the inflow and outflow regions are respectively expressed as follows:

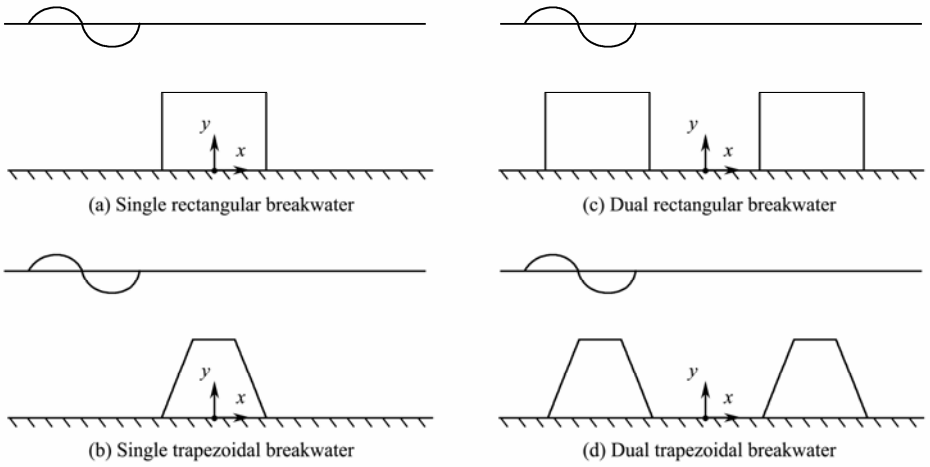

Fig.1 Breakwater systems considered in this study.

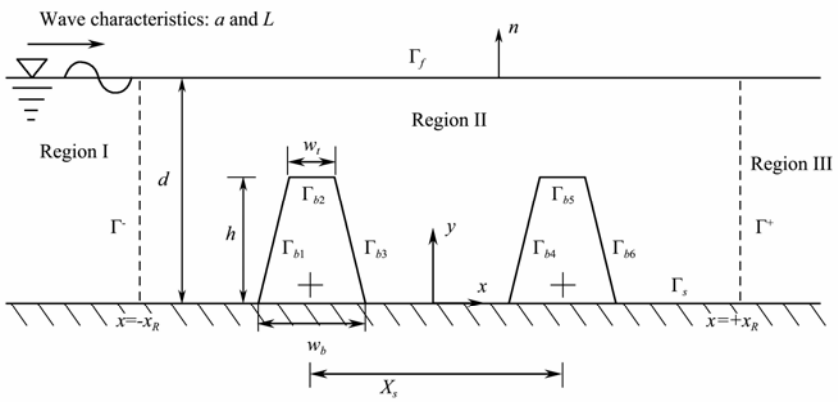

Fig.2 Problem definitions for the breakwater system.

$$\frac{\partial(\phi-\phi_I)}{\partial n}-ik(\phi-\phi_I)=0 \text{ radiation condition at } x\to-\infty \quad \text{(boundary } \Gamma^-\text{)}, \quad (5)$$

$$\frac{\partial(\phi)}{\partial n}-ik(\phi)=0 \text{ radiation condition at } x\to+\infty, \quad \text{(boundary } \Gamma^+\text{)}, \quad (6)$$

where ϕ_I is the incident velocity potential.

The radiation conditions in the infinite strip problem are treated by transferring the far-field potentials at two fictitious vertical boundaries at finite distances $x=-x_R$ and $x=+x_R$, which represent the left (Γ^-) and right (Γ^+) boundaries, respectively, of the fluid domain. The analytical series at these boundaries are given by the following:

$$\phi^-=\phi_I+A^-\frac{\cosh(ky)}{\sinh(kd)}e^{-ik(x+x_R)} \text{ and } \frac{\partial\phi^-}{\partial n}=-\frac{\partial\phi^-}{\partial x} \quad \text{for } x=-x_R \text{ (boundary } \Gamma^-\text{)}, \quad (7a)$$

$$\phi^+=A^+\frac{\cosh(ky)}{\sinh(kd)}e^{ik(x-x_R)} \text{ and } \frac{\partial\phi^+}{\partial n}=\frac{\partial\phi^+}{\partial x} \quad \text{for } x=+x_R \text{ (boundary } \Gamma^+\text{)}, \quad (7b)$$

where A^- and A^+ are unknown complex coefficients to be determined. The disturbances are guaranteed to be outgoing waves only (see for example Chioukh *et al.*, 2017; Bakhti *et al.*, 2017). The incident velocity potential is defined as follows:

$$\phi_I=-\frac{aL}{T}\frac{\cosh(ky)}{\sinh(kd)}e^{ik(x+x_R)}. \quad (8)$$

The unique matching conditions at the interfaces Γ^- and Γ^+ of the flow regions ensure the smooth transfer of the mass flow from one region to the next. Once the potentials ϕ^- and ϕ^+ are calculated by satisfying the radiation boundary conditions of Eqs. (5) and (6), they are matched to those of Eqs. (7a) and (7b), respectively; then, the unknown coefficients A^- and A^+ are evaluated following the method of Yueh and Chuang (2012):

$$A^-=-(-\frac{aL}{T})+\frac{k}{N_0\cosh(kd)}\int_0^d\phi^-(-x_R,y)\mathrm{d}y, \quad (9a)$$

$$A^+=\frac{k}{N_0\cosh(kd)}\int_0^d\phi^+(+x_R,y)\mathrm{d}y, \quad (9b)$$

where

$$N_0=\frac{1}{2}\left(1+\frac{2kd}{\sinh(2kd)}\right).$$

The reflection and transmission coefficients (*Cr* and *Ct*) are respectively determined from the following expressions (see for example Chioukh *et al.*, 2017; Bakhti *et al.*, 2017):

$$Cr=|A_0^-|\frac{T}{aL} \text{ and } Ct=|A_0^+|\frac{T}{aL}. \quad (10)$$

3 Numerical Solution by the ISBM

For the numerical solution, the total boundary of the whole computational domain is discretized for single and double breakwaters (Fig.3).

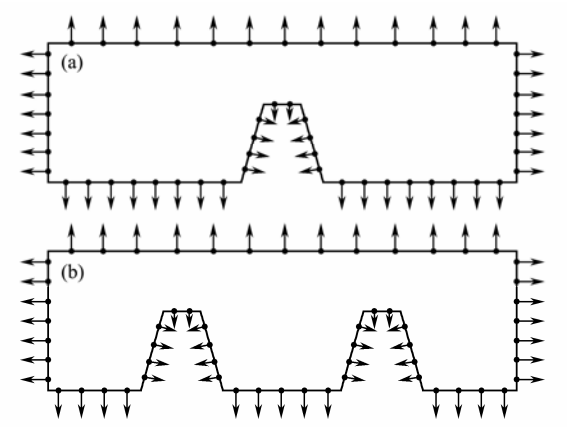

Fig.3 Domain discretization for (a) single and (b) double breakwaters.

In the ISBM, the nodal values of the potentials and their fluxes are expressed as linear combinations of the fundamental solutions and their derivatives (Chen and Gu, 2012; Gu *et al.*, 2012; Gu and Chen, 2013):

$$\phi(x^i)=\sum_{j=1,i\neq j}^{N}\alpha^jQ(x^i,s^j)+\alpha^i\phi_{ii}, \quad (11)$$

$$q(x^i)=\frac{\partial\phi(x^i)}{\partial n_{x^i}}=\sum_{j=1,i\neq j}^{N}\alpha^j\frac{\partial Q(x^i,s^j)}{\partial n_{x^i}}+\alpha^iq_{ii}, \quad (12)$$

where α^j is an unknown coefficient to be determined, x^i and s^j are the collocation points (x_i, y_i) and source points (x'_j, y'_j), respectively, and N is the total number of points. $\phi(x^i)$ refers to the essential boundary condition (Dirichlet), $q(x^i)$ denotes the natural boundary condition (Neumann), and n_{x^i} is the normal at the collocation point x^i. The coefficients ϕ_{ii} and q_{ii} are source intensity factors corresponding to the fundamental solution and its derivative, respectively. $Q(x^i, s^j)$ is the fundamental solution of the 2D Laplace equation. This variable depends only on the Euclidean distance $r_{ij}=|x^i-s^j|$ between the collocation point x^i and source point s^j, *i.e.*,

$$r_{ij}=\sqrt{(x_i-x'_j)^2+(y_i-y'_j)^2},$$

and is given together with its normal derivative as follows:

$$Q(x^i,s^j)=\frac{1}{2\pi}\ln\left(\frac{1}{r_{ij}}\right), \quad (13a)$$

$$\frac{\partial Q(x^i,s^j)}{\partial n_{x^i}}=-\frac{[(nx_{x^i})(x_i-x'_j)+(ny_{x^i})(y_i-y'_j)]}{2\pi(r_{ij})^2}, \quad (13b)$$

where nx_{x^i} and ny_{x^i} are the components of the normal at the collocation point x^i.

The coefficients ϕ_{ii} and q_{ii} are the diagonal elements of the ISBM interpolation matrices. These variables arise when the collocation and source points coincide ($x^i=s^j$). Direct evaluation of these coefficients is unfeasible given the singularities inherent in the fundamental solution and its derivative. In this study, the coefficient ϕ_{ii} is evaluated by the integration of the fundamental solution on the line segments, leading to simple analytical expression, as in the works of Brebbia and Dominguez (1992) and Gu and Chen (2014):

$$\phi_{ii}=\frac{1}{\ell_i}\int_{\Gamma_s}Q(x^i,s)\mathrm{d}\Gamma_s=\frac{1}{2\pi}\left[\ln\left(\frac{2}{\ell_i}\right)+1\right]. \quad (14)$$

For the coefficient q_{ii}, a simple expression is derived by Gu *et al.* (2012) using the regularization process of subtracting and adding-back to remove singularities:

$$q_{ii}=-\frac{1}{\ell_i}\sum_{j=1,i\neq j}^{N}\ell_j\frac{\partial Q(x^i,s^j)}{\partial n_{s^j}}, \quad (15)$$

where ℓ_i and ℓ_j represent the half distances between the collocations points (x^{i-1} and x^{i+1}) and the source points (s^{j-1} and s^{j+1}), respectively. n_{s^j} is the normal at the source point s^j.

The boundary conditions given by Eqs. (2)–(6) are satisfied by a linear combination of Eqs. (11) and (12). The discretization process leads to the following system of equations.

For nodes $x^i\in\Gamma_f$ (the free surface boundary),

$$\sum_{j=1,i\neq j}^{N}\alpha^j\left(\frac{\partial Q(x^i,s^j)}{\partial n_{x^i}}-\frac{\sigma^2}{g}Q(x^i,s^j)\right)+\alpha^i\left(q_{ii}-\frac{\sigma^2}{g}\phi_{ii}\right)=0. \quad (16)$$

For nodes $x^i\in\Gamma^-$ (the radiation boundary at $x=-x_R$),

$$\sum_{j=1,i\neq j}^{N}\alpha^j\left(\frac{\partial Q(x^i,s^j)}{\partial n_{x^i}}-i.k.Q(x^i,s^j)\right)+\alpha^i\left(q_{ii}-ik\phi_{ii}\right)=\frac{\partial\phi_I(x^i)}{\partial n_{x^i}}-ik\phi_I(x^i). \quad (17)$$

For nodes $x^i\in\Gamma^+$ (the radiation boundary at $x=+x_R$),

$$\sum_{j=1,i\neq j}^{N}\alpha^j\left(\frac{\partial Q(x^i,s^j)}{\partial n_{x^i}}-ikQ(x^i,s^j)\right)+\alpha^i\left(q_{ii}-ik\phi_{ii}\right)=0. \quad (18)$$

For nodes $x^i\in\Gamma_s$ and Γ_b (seabed and the breakwater boundaries),

$$\sum_{j=1,i\neq j}^{N}\alpha^j\frac{\partial Q(x^i,s^j)}{\partial n_{x^i}}+\alpha^i q_{ii}=0. \quad (19)$$

The resulting discretized Eqs. (16)–(19) are written in a more compact matrix form as follows:

$$\left[\mathrm{H}_{ij}\right]_{N\times N}\left\{\alpha^j\right\}_N=\left\{\mathrm{B}_i\right\}_N,\ i,j=1,2,\cdots,N, \quad (20)$$

where N specifies the total number of nodes on the whole domain boundaries, *e.g.*, $N=N^f+N^-+N^++N^b+N^s$, where N^f, N^-, N^+, N^b and N^s are the number of nodes on the boundaries Γ_f, Γ^-, Γ^+, Γ_b, and Γ_s, respectively. The algebraic system of equations expressed by Eq. (20) is solved numerically using a Gaussian elimination algorithm to yield the vector of unknown $\{\alpha^i\}$. The potential and its derivative at the nodes are then computed using Eqs. (11) and (12).

4 Validation of the Numerical Method

The sensitivity of the numerical results in terms of conservation of energy with respect to the total number of boundary nodes N and the position $x=\pm x_R$ of the vertical fictitious boundaries is tested for single and dual rectangular breakwaters for two values of the relative water depth: $kd=0.5$, and $kd=4$. This process ensures that tests are applicable for small and large values of kd. Energy conservation is expressed as $|1-(Cr)^2-(Ct)^2|$ and can be regarded as an error indicator of the numerical solutions. Fig.4(a) displays the results of errors against N for a single breakwater with relative breakwater height $h/d=0.75$ and relative breakwater width $w/d=1$. Fig.4(b) shows the results for the dual breakwaters separated by a distance X_S, with $h/d=0.75$, and $w/d=1$. To plot the results of the errors with respect to the location of the vertical fictitious boundaries, the criteria of Li *et al.* (2016) are followed. Fig.5(a) plots the errors against the quantity $2x_R/w$ for a single breakwater with $N=400$ nodes, whereas Fig.5(b) presents the plot against the quantity $[2x_R-(X_S-w)]/2w$ for dual breakwaters with $N=600$ nodes.

In all the numerical computations to follow and based on the results in Figs.4 and 5, the whole boundary of the computational domain is discretized with 400 source nodes for single breakwaters and 600 source nodes for dual breakwaters. This process would ensure that the computational errors remain small and below 10^{-2}, provided that the vertical boundaries are selected, such that $(2x_R/w_b)\geq 3$, and $[2x_R-(X_S-w_b)]/2w_b\geq 3$ for single and dual breakwaters, respectively. For rectangular breakwaters, w_b is adequately exchanged by w.

To demonstrate the validity of the present method, the numerical results of the ISBM for a number of limiting cases are compared against those of other investigators. The first case examined is a bottom-standing single impermeable rectangular breakwater for $h/d=0.75$, and $w/d=1$. This case was previously studied by Abul-Azm (1994) using the EFEM and Chen *et al.* (2011) using both the BEM and RMM. Fig.6 presents the variations in the coef-

ficients of reflection and transmission (*Cr* and *Ct*, respectively) with respect to *kd*, including those of the present investigation. A high agreement is observed among the results of all methods. Noticeably, at large values of *kd*, the results of the ISBM still follow those of the EFEM and BEM, but those of the RMM exhibit fluctuations.

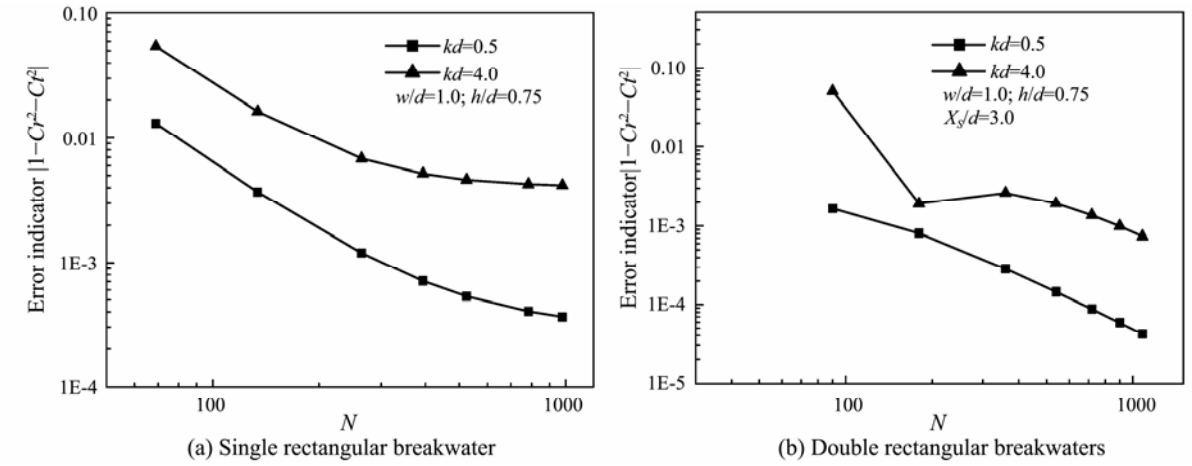

Fig.4 Error indicator versus the number of boundary nodes.

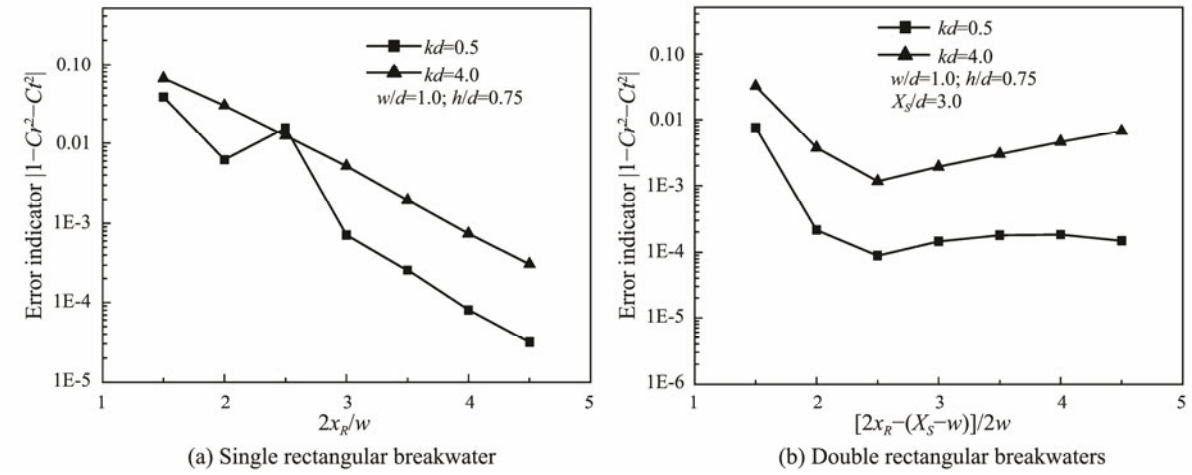

Fig.5 Error indicator versus the location of vertical fictitious boundaries.

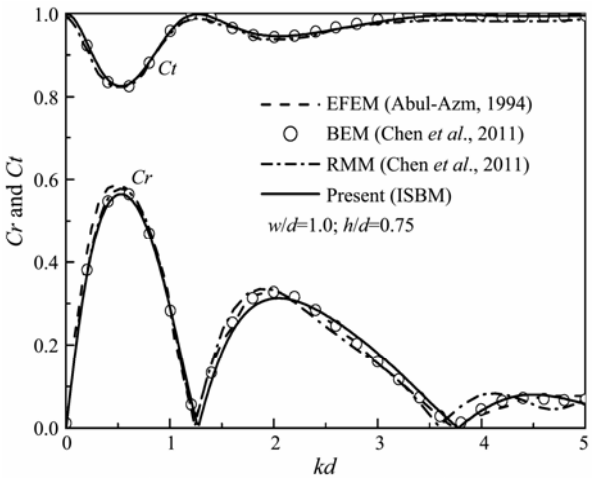

Fig.6 Variations in *Cr* and *Ct versus kd* for single rectangular breakwater under different methods.

The second case examined is a structure of bottom-standing dual impermeable rectangular breakwaters, such that $h/d=0.5$, $w/d=0.5$, and $X_S/d=3$. For the same conditions, the trapezoidal impermeable breakwaters ($w_b/d=0.5$, and $w_t/w_b=0.5$) are also inspected. These cases were previously studied experimentally by Cho *et al.* (2004), who also provided analytical solutions using the EFEM. Similarly, Ouyang *et al.* (2016) carried out numerical tests on the same cases using the RMM. Fig.7 displays the results of the reflection coefficients (*Cr*), including those of the present study, for rectangular breakwaters; Fig.8 shows those for the trapezoidal breakwaters. In general, the results of all methods are in close agreement.

5 Results and Discussion

Given the large number of parameters on hand, a considerable number of cross-correlations must be investigated. For single breakwaters, the parameters of interest include *kd*, *h*/*d*, and *w*/*d* (w_b/d and w_t/w_b for trapezoidal breakwaters), whereas X_S/L is the parameter of interest for dual breakwaters. All these parameters must be cross-

correlated to reveal meaningful conclusions. In this work, only a subset of the data gathered from this study is shown.

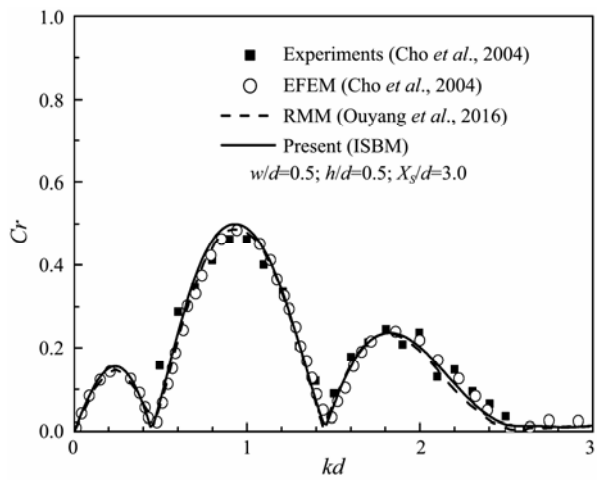

Fig.7 Variation in *Cr versus kd* for double rectangular breakwaters under different methods.

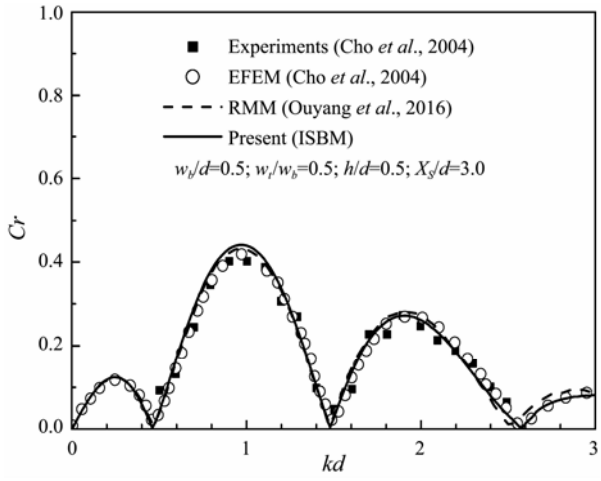

Fig.8 Variation in *Cr versus kd* for double trapezoidal breakwaters under different methods.

5.1 Single Breakwaters

Fig.9 shows the variations in the values of *Cr* and *Ct versus* the *kd* for different values of *h*/*d*. The results in Fig.9(a) for rectangular breakwater with $w/d = 1$ show the occurrence of several peaks for certain values of *kd*. The larger primary peaks occur at lower values of *kd*. Increasing the breakwater height increases the reflection and lowers the transmission, indicating that elevated breakwaters provide better shelter. For a trapezoidal breakwater with a base of the same width as the rectangular breakwater ($w_b/d = 1$) and top width half of the width of the base ($w_t/w_b = 0.5$), the results in Fig.9(b) also show that increasing the height of the breakwater increases the reflection and lowers the transmission. However, although the primary peaks have slightly decreased compared with those of the rectangular breakwater, the spectrum width around these primary peaks have broadened, suggesting that the trapezoidal breakwater is a better alternative than the rectangular breakwater in terms of shoreline protection.

Fig.10 shows the variations in the values of *Cr* and *Ct* versus *kd* for different values of the breakwater width. The results in Fig.10(a) for rectangular breakwater with $h/d = 0.75$ show that increasing the breakwater width leads to the appearance of more peaks in *Cr* and *Ct* at different values of *kd*. For a particular width of the breakwater, the magnitudes of these peaks decrease with the increase in *kd*. By increasing the width, the reflection of the major peaks increases, whereas the transmission decreases. However, the change shows no significance as in the case for increasing breakwater heights. Fig.10(b) shows the same effect for a trapezoidal breakwater with a base of the same width as the rectangular breakwater and top width half of the base width ($w_t/w_b = 0.5$). Furthermore, the primary peaks have slightly decreased compared with those of the rectangular breakwater, but the spectrum width has expanded especially for shallow and intermediate waters ($kd < 3.14$). These results indicate the superior wave energy reflected by the trapezoidal breakwater.

5.2 Double Breakwaters

The double breakwaters in this study are considered to be of the same height and width. Fig.11 shows the varia-

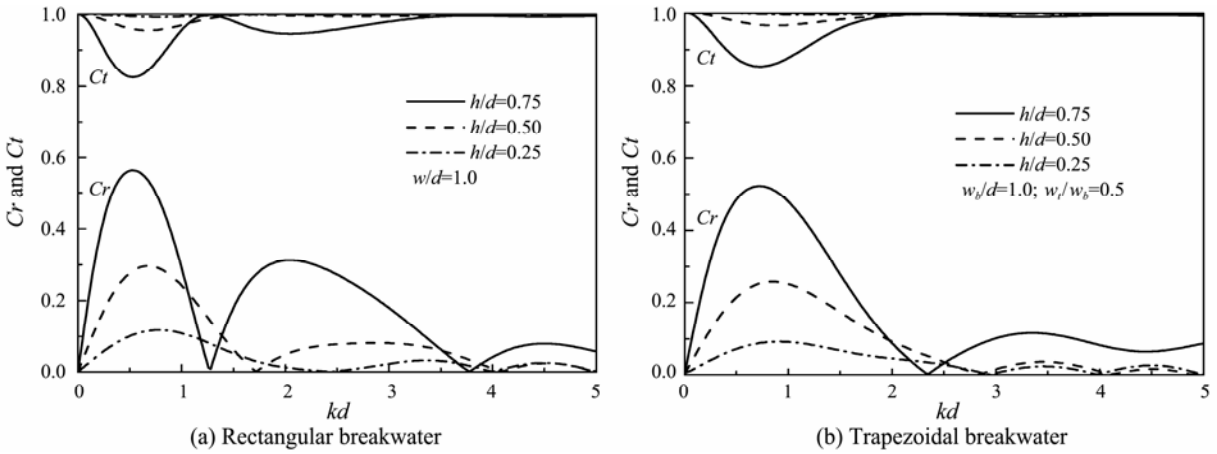

Fig.9 Variations in *Cr* and *Ct versus kd* for different values of *h*/*d*.

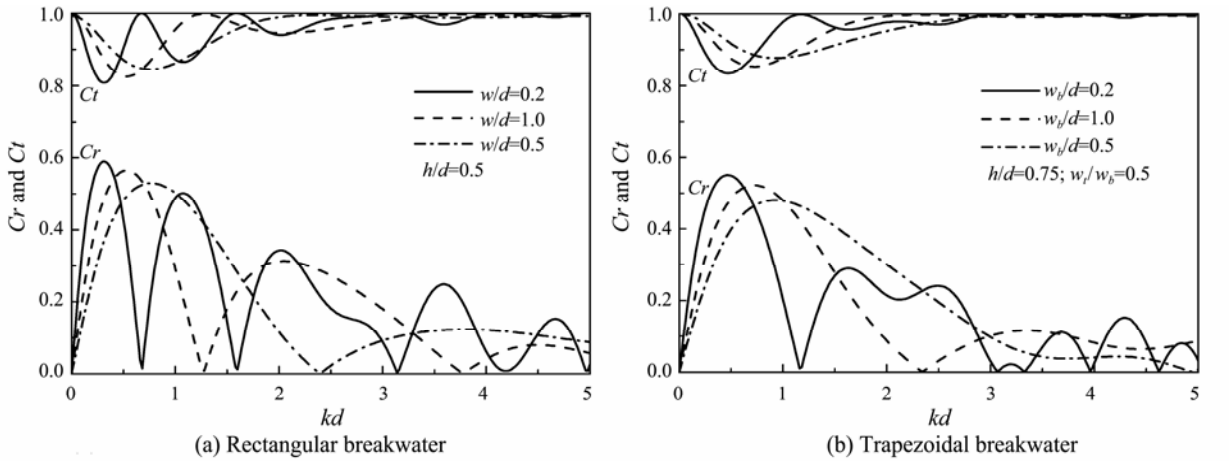

Fig.10 Variations in *Cr* and *Ct versus kd* for different values of the breakwater widths.

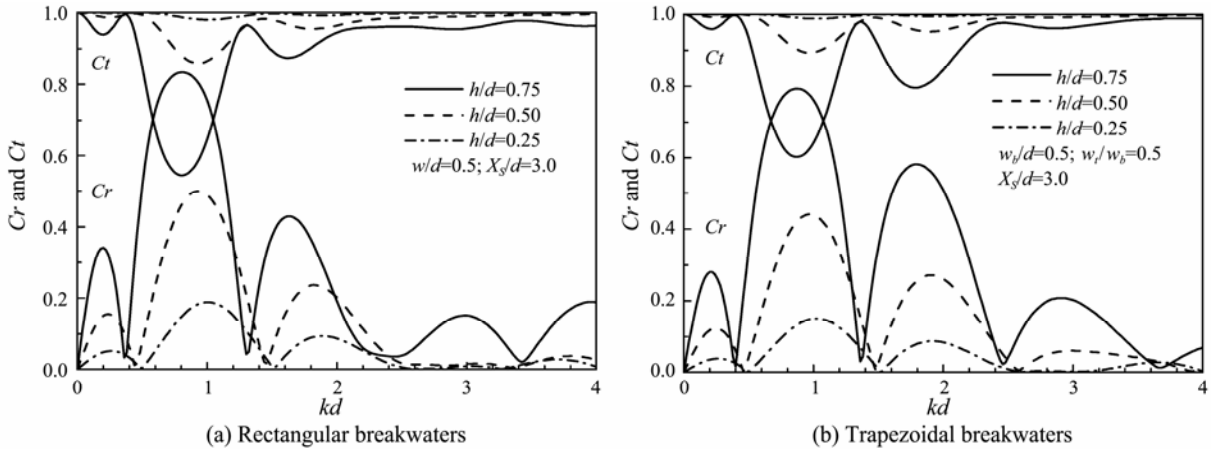

Fig.11 Variations in *Cr* and *Ct versus kd* for different values of *h/d.*

tions in *Cr* and *Ct versus kd* for different values of *h*/*d*. Fig.11(a) displays the occurrence of several peaks near the integer values of *kd* for rectangular breakwaters with $w/d=0.5$ and $X_S/d=3$. The larger primary peaks occur at *kd* around 1. The secondary peaks are a bit distant from a *kd* of 2. Increasing the breakwater height increases the reflection and lowers the transmission. For trapezoidal breakwaters with a base of the same width as the rectangular breakwaters ($w_b/d=0.5$) and top width half of the width of the base ($w_t/w_b=0.5$), the results in Fig.11(b) show similar trends. However, all peaks occur much closer to the integer values of *kd*. Although the primary peaks have slightly decreased compared with those of the rectangular breakwater, the secondary and tertiary peaks have increased, leading to the broader width of the spectrum and suggesting the better performance of the trapezoidal breakwater. The overall width of both breakwaters ($2w/d=1$ for rectangular and $2w_b/d=1$ for trapezoidal) is similar to the single breakwater presented in Fig.9. However, a much better performance is observed with using two breakwaters separated by a distance than when using a single breakwater. By using a system of dual breakwaters, the reflections increase, and the transmissions decrease. This result is demonstrated for the trapezoidal breakwaters.

Fig.12 shows the variations in *Cr* and *Ct versus* the *kd* for different values of the breakwater widths. As shown in Fig.12(a), the results for rectangular breakwaters with $h/d=0.75$ and $X_S/d=3$ indicate that the primary peaks are of nearly similar magnitudes. Hence, they are unremarkably affected by the increase in *w*/*d*. The secondary and tertiary peaks are of different magnitudes, but those with a larger *w*/*d* are not necessarily the largest. This finding suggests that increasing the width of the breakwater causes no improvement in the performance of the system. Fig.12(b) shows the similar trends observed for trapezoidal breakwaters with a base of the same width as the rectangular breakwaters and $w_t/w_b=0.5$. The spectrum shows no remarkable difference from that of the rectangular breakwaters. Thus, adopting trapezoidal breakwaters is advised, bearing in mind the massive conservation in terms of construction time and costs. Comparing the results in Fig.12 for dual breakwaters and those in Fig.10 for single breakwaters, using two breakwaters separated by a distance performs much better than using a single breakwater due to increased reflections and decreased transmissions.

Fig.13 shows the effect of varying the distance between the breakwaters for different values of *h/d*. The distance between breakwaters is expressed in terms of twice the relative spacing $2X_S/L$. Fig.13(a) presents the results for the rectangular breakwaters with $w/d=1$ and $kd=1$,

whereas Fig.13(b) depict the findings for the trapezoidal breakwaters with $w_b/d=1$ and $w_t/w_b=0.5$. All the *Cr* and *Ct* curves vary periodically with the increasing values of $2X_S/L$. For low breakwaters ($h/d=0.25$), the zero values of *Cr* and *Ct* occur at $2X_S/L\approx0.5+n$ ($n=1, 2, 3,\cdots$). On the other hand, the maximum values of *Cr* (corresponding to the minimum values of *Ct*) occur at integer values of $2X_S/L$, *i.e.*, $2X_S/L\approx n$ ($n=1, 2, 3,\cdots$). This finding is in accordance with those of previous studies, for example, that of Ouyang *et al.* (2016), who observed that when the incident wave length is twice as long as the spacing between the crests of the breakwaters, Brag resonance occurs, leading to amplification of reflection and subsequent reduction in the transmitted waves. When the height of the breakwaters is increased, reflection raises, and transmission decreases, but the values of $2X_S/L$ at which the optimum and zero values occur reduce. For the trapezoidal breakwaters, similar trends are shown, but the optimums are amplified as they are absent at the same *kd* values compared with those of the rectangular breakwaters.

Fig.14 shows the variations in *Cr* and *Ct versus* $2X_S/L$ for different breakwater widths. Fig.14(a) displays the results for the rectangular breakwaters with $h/d=0.5$ and $kd=1$, whereas Fig.14(b) illustrates the findings for the trapezoidal breakwaters with a base of the same width as the rectangular breakwaters and $w_t/w_b=0.5$. Again, all the *Cr* and *Ct* curves vary in a periodic fashion. The results also confirm that the increase in the breakwater widths causes no remarkable effect on the variations in *Cr* and *Ct*.

6 Conclusions

The work carried out in this numerical study has employed the improved version of the original SBM (ISBM) to evaluate the hydrodynamic quantities of reflection and transmission of bottom-standing submerged impermeable breakwaters in regular normally incident waves. Both single and dual prismatic breakwaters of rectangular and trapezoidal forms were examined. The correctness and accuracy of the results of the present method were confirmed by comparison with previously published results of other methods, including the EFEM, BEM, RMM, and experimental data. The effects of major design parameters, including breakwater height, width, and spacing, were investigated for several wave conditions. The results demonstrate that in places where only partial protection from waves is required, submerged breakwaters can be used successfully, as they can substantially attenuate

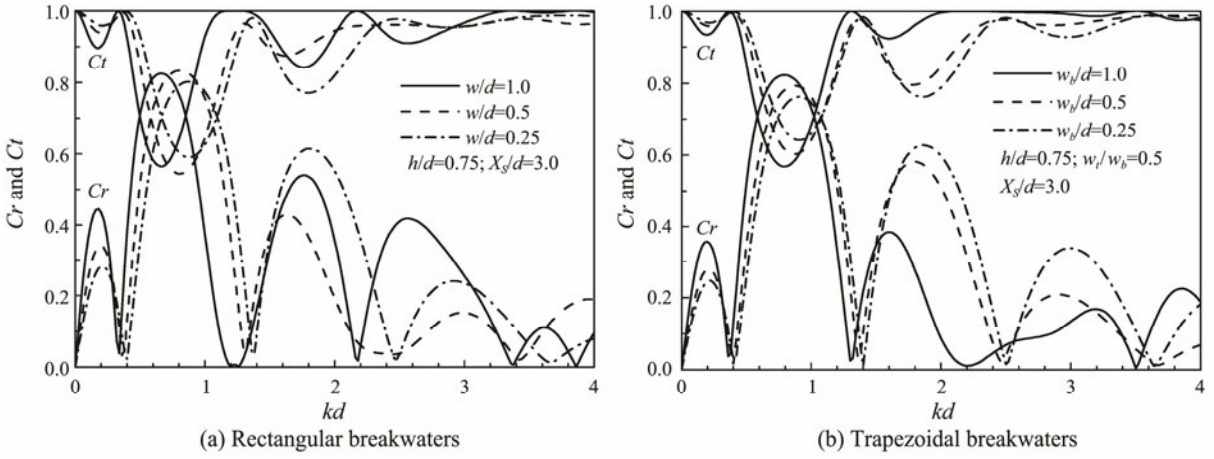

Fig.12 Variations in *Cr* and *Ct versus kd* for different values of breakwater widths.

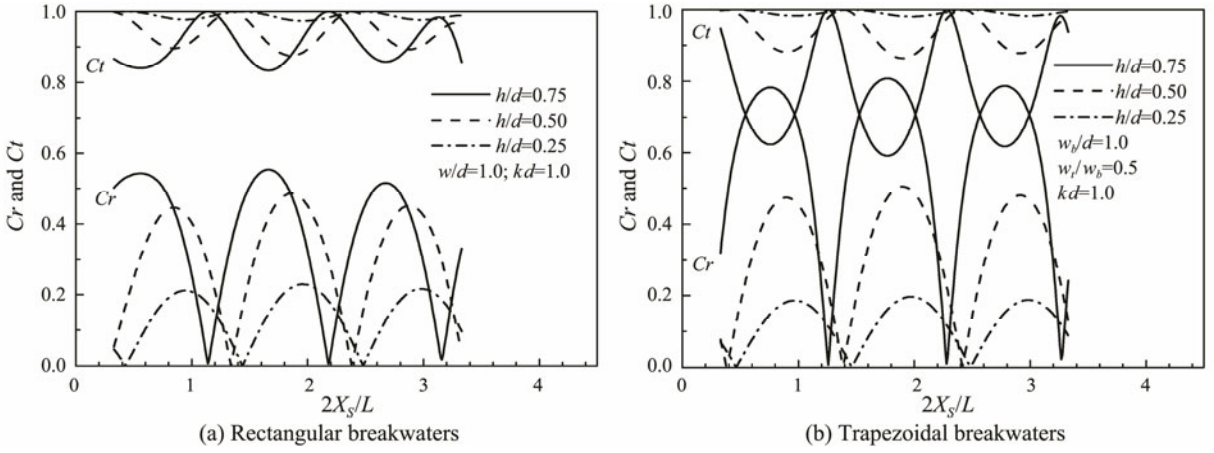

Fig.13 Variations in *Cr* and *Ct versus* $2X_S/L$ for different values of h/d.

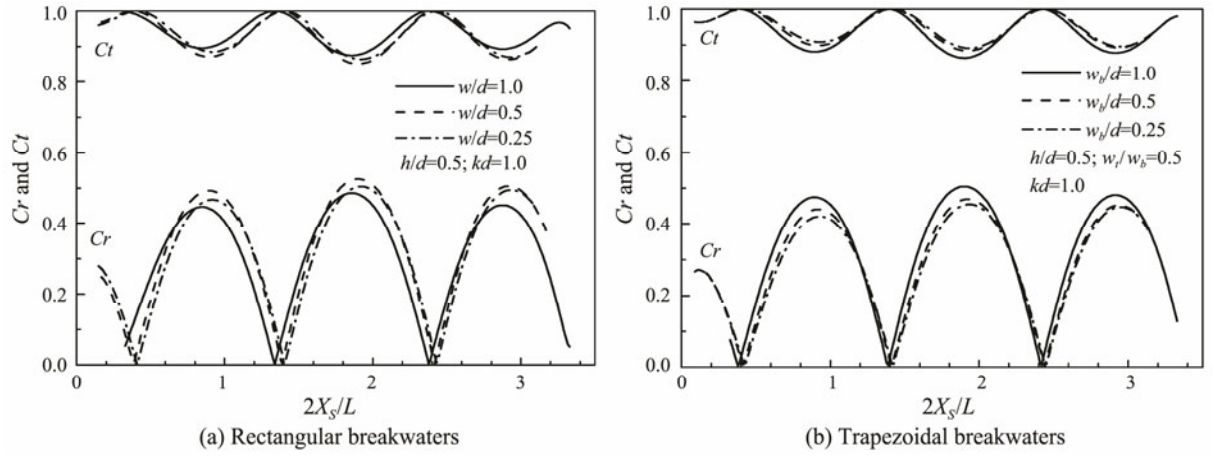

Fig.14 Variations in *Cr* and *Ct* versus $2X_S/L$ for different breakwater widths.

waves. Dual breakwaters were found to perform better than single breakwaters. The resonant reflections and transmissions are amplified with the increase in both the height and width of the breakwaters. Nevertheless, the width was found to feature an extremely limited effect. The reflection and transmission coefficients vary periodically with the spacing relative to the wavelength. Optimum values occur at integer values twice the relative spacing to the wavelength. In the trapezoidal breakwaters, the hydrodynamic quantities exhibit broader spectra than those in the rectangular breakwaters, suggesting the better performance of trapezoidal breakwaters. Therefore, adopting trapezoidal breakwaters is recommended for shoreline protection, bearing in mind the considerable savings in terms of construction time and costs.

Acknowledgements

This study was supported by the Direction Général des Enseignements et de la Formation Supérieure of Algeria under Grant CNEPRU number G0301920140029.

References

Abul-Azm, A. G., 1994. Diffraction through wide submerged breakwaters under oblique waves. *Ocean Engineering*, **21** (7): 683-706.

Bakhti, Y., Chioukh, N., Hamoudi, B., and Boukhari, M., 2017. A multi-domain boundary element method to analyze the reflection and transmission of oblique waves from double porous thin walls. *Journal of Marine Science and Application*, **16** (3): 276-285.

Brebbia, C. A., and Dominguez, J., 1992. *Boundary Elements: An Introductory Course*. 2nd edition. Computational Mechanics Publications, WIT Press, Southampton and Boston, 328pp.

Chen, K. H., Lu, M. C., and Hsu, H. M., 2011. Regularized meshless method analysis of the problem of obliquely incident water wave. *Engineering Analysis with Boundary Elements*, **35** (3): 355-362.

Chen, W., and Fu, Z., 2010. A novel numerical method for infinite domain potential problems. *Chinese Science Bulletin*, **55** (16): 1598-1603.

Chen, W., and Gu, Y., 2012. An improved formulation of singular boundary method. *Advances in Applied Mathematics and Mechanics*, **4** (5): 543-558.

Chen, W., and Wang, F. Z., 2010. A method of fundamental solutions without fictitious boundary. *Engineering Analysis with Boundary Elements*, **34** (5): 530-532.

Chen, W., Zhang, J. Y., and Fu, Z. J., 2014. Singular boundary method for modified Helmholtz equations. *Engineering Analysis with Boundary Elements*, **44**: 112-119.

Chioukh, N., Çevik, E., and Yüksel, Y., 2017. Reflection and transmission of regular waves from/through single and double perforated thin walls. *China Ocean Engineering*, **31** (4): 466-475.

Cho, Y. S., Lee, J. I., and Kim, Y. T., 2004. Experimental study of strong reflection of regular water waves over submerged breakwaters in tandem. *Ocean Engineering*, **31** (10): 1325-1335.

Dattatri, J., Raman, H., and Shankar, N. J., 1978. Performance characteristics of submerged breakwaters. In: *Proceedings of the 16th International Conference on Coastal Engineering*. ASCE, Hamburg, Germany, **16**: 2153-2171.

Fairweather, G., and Karageorghis, A., 1998. The method of fundamental solutions for elliptic boundary value problems. *Advances in Computational Mathematics*, **9**: 69-95.

Fu, Z. J., Chen, W., Lin, J., and Cheng, A. H. D., 2015. Singular boundary method for various exterior wave applications. *International Journal of Computational Methods*, **12** (2): 1550011.

Gu, Y., and Chen, W., 2013. Infinite domain potential problems by a new formulation of singular boundary method. *Applied Mathematical Modelling*, **37** (4): 1638-1651.

Gu, Y., and Chen, W., 2014. Recent advances in singular boundary method for ultra-thin structural problems. *WIT Transactions on Modelling and Simulation, Boundary Elements and Other Mesh Reduction Methods XXXVI*, **56**: 233-243.

Gu, Y., Chen, W., and Zhang, J. Y., 2012. Investigation on near-boundary solutions by singular boundary method. *Engineering Analysis with Boundary Elements*, **36** (8): 1173-1182.

Hsu, T. W., Chang, H. K., and Hsieh, C. M., 2002. Bragg reflection of waves by different shapes of artificial bars. *China Ocean Engineering*, **16** (3): 21-30.

Koley, S., Behera, H., and Sahoo, T., 2015a. Oblique wave trapping by porous structures near a wall. *Journal of Engineering Mechanics*, *ASCE*, **141** (3): 04014122.

Koley, S., Sarkar, A., and Sahoo, T., 2015b. Interaction of gravity waves with bottom-standing submerged structures having perforated outer-layer placed on a sloping bed. *Applied Ocean*

Research, **52**: 245-260.

Li, J., Fu, Z., and Chen, W., 2016. Numerical investigation on the obliquely incident water wave passing through the submerged breakwater by singular boundary method. *Computers and Mathematics with Applications*, **71** (1): 381-390.

Liu, Y., Li, H., and Zhu, L., 2016. Bragg reflection of water waves by multiple submerged semi-circular breakwaters. *Applied Ocean Research*, **56**: 67-78.

Ouyang, H. T., Chen, K. H., and Tsai, C. M., 2016. Wave characteristics of Bragg reflections from a train of submerged bottom breakwaters. *Journal of Hydro-Environment Research*, **11**: 91-100.

Twu, S. W., and Liu, C. C., 2004. Interaction of non-breaking regular waves with a periodic array of artificial porous bars. *Coastal Engineering*, **51** (3): 223-236.

Young, D. L., Chen, K. H., and Lee, C. W., 2005. Novel meshless method for solving the potential problems with arbitrary domains. *Journal of Computational Physics*, **209** (1): 290-321.

Yueh, C. Y., and Chuang, S. H., 2012. A boundary element model for a partially piston-type porous wave energy converter in gravity waves. *Engineering Analysis with Boundary Elements*, **36** (5): 658-664.

Zhao, Y., Li, H. J., and Liu, Y., 2017. Oblique wave scattering by a submerged porous breakwater with a partially reflecting sidewall. *Journal of Marine Science and Technology*, **25** (4): 383-392.

(Edited by Xie Jun)